Implications of Underground Nuclear Explosion Cavity Evolution for Radioxenon Isotopic Composition

Yunwei Sun, Charles R. Carrigan, Eric Pili, Tarabay Antoun

Implications of Underground Nuclear Explosion Cavity Evolution for Radioxenon Isotopic Composition

Yunwei Sun,[1] Charles R. Carrigan,[2] Eric Pili,[3,4] and Tarabay Antoun[1]

Abstract—Isotopic ratios of radioxenons sampled in the atmosphere or subsurface can be used to verify the occurrence of an underground nuclear explosion (UNE). Differences in the half-lives of radioactive xenon precursors and their decay-chain networks produce different time-dependent concentration profiles of xenon isotopes allowing isotopic ratios to be used for tracking UNE histories including estimating the time of detonation. In this study, we explore the potential effects of post-detonation cavity processes: precipitation of iodine precursors, gas seepage, and prompt venting on radioxenon isotopic evolution which influences UNE histories. Simplified analytical models and closed-form solutions yielding a potentially idealized radioactive decay/ingrowth chain in a closed and well-mixed system typically have limited application by not including the partitioning of the radionuclide inventory between a gas phase and rock melt created by the detonation and by ignoring gas transport from the cavity to host rock or ground surface. In reality, either subsurface transport or prompt release that is principally responsible for gas signatures violates the closed-system (or batch-mode) assumption. A closed-form solution representing time-dependent source-term activities is extended by considering the cavity partitioning process, slow seepage, and/or prompt release of gases from the cavity and applied to realistic systems.

Keywords: Radioactive decay, transport, underground nuclear explosion, noble gas, xenon isotopic evolution.

1. Introduction

Monitoring for underground nuclear explosions (UNEs) uses atmospheric detection of radionuclide gases released by either seepage or prompt venting at the ground surface of the test site following a UNE

[1] Lawrence Livermore National Laboratory, Livermore, CA 94550, USA. E-mail: sun4@llnl.gov

[2] M.H. Chew & Associates, Livermore, CA 94550, USA.

[3] CEA, DAM, DIF, 91297 Arpajon, France.

[4] Université de Paris, Institut de physique du globe de Paris, CNRS, 75005 Paris, France.

(Saey & De Geer, 2005; Carrigan et al., 2016). Advances in the technology for measuring radioxenon concentrations have enhanced the detection of both UNE signatures and the global background of radioxenons produced by civilian facilities including nuclear reactors and medical isotope production plants (Le Petit et al., 2015; Achim et al., 2016; Gueibe et al., 2017; Haas et al., 2017; Hoffman & Berg, 2018). Isotopic ratios of radioxenons (e.g., $^{[131m\ 133m\ 133\ 135]}$Xe) have been assessed as indicators of UNEs (Bowyer et al., 1998; Saey & De Geer, 2005; Kalinowski & Pistner, 2006; Kalinowski et al., 2010; Saey et al., 2010; Kalinowski, 2011; Galan et al., 2018). Different half-lives of these xenon isotopes originating from three different decay networks can produce detectable signals (Saey et al., 2010; Sloan et al., 2016; Bowyer, 2020). The radioactivity of each xenon isotope is characterized by a unique dependence on time as a result of its decay chain and half-lives of precursors reaching peak activity at a distinctive time. In the absence of physical partitioning of the radioactive inventory in the post-detonation cavity, seepage, and prompt venting, radioxenon profiles will only reflect the mechanism of radioactive decay and ingrowth in a closed and well-mixed (i.e., batch-mode) system (De Geer, 2013; Kalinowski & Liao, 2014; Yamba et al., 2016).

A realistic UNE system, in general, may be composed of a cavity and melt puddle (Fig. 1) with possible post-detonation partitioning of radionuclides from the gas-filled cavity into the underlying puddle of molten rock (R), gas seepage into the fractured zone of containment (S), and/or prompt venting of larger volumes of cavity gas (V) either of which is potentially capable of producing detectable xenon signatures at ground surface or downwind. In the
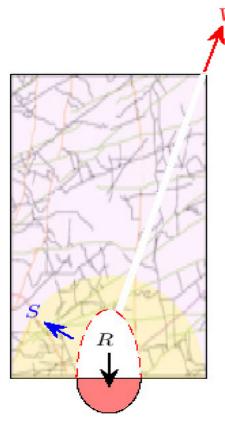
Figure 1
Vertical cross-section of conceptual model with rainout (R) from the cavity (white) to melt puddle (red), seepage (S) from the cavity to host rock (yellow), and prompt release (V) from the cavity to ground surface (in a user-defined time period). The back diffusion from melt puddle to cavity is neglected

context of our cavity-melt partitioning model (Carrigan et al., 2020; Sun et al., 2021), the detonation system following a UNE is described by several interacting subsystems or compartments (e.g., cavity, rock-melt puddle, and host rock). Each compartment may exchange radionuclides with other compartments. Although the slow seepage from the cavity to host rock was considered by Sun et al. (2021) in the analytical solution of generalized systems, prompt venting during a specified period of time has not been included. In the fully coupled numerical model of multiphase transport and radionuclide decay and ingrowth (Carrigan et al., 2016; Bourret et al., 2021), the transport of xenon isotopes produced from chain reactions in the cavity was accurately described. However, the signature of promptly vented xenons was approximated using the xenon evolution in the

cavity directly (Carrigan et al., 2021). Since the prompt venting alters mass balance in the cavity, a full-scale mass exchange needs to be considered among all compartments. In this paper, we derived a closed-form solution to a full-scale model considering time-dependent mass exchanges among interactive compartments: (1) thermally induced condensation (rainout) of refractory iodine precursors from cavity to rock melt, (2) seepage of cavity gases into a fractured containment zone, and (3) prompt venting of cavity gases to ground surface. The back diffusion from melt puddle to cavity is not considered because of its low gas flux compared to other exchange processes.

2. Model and Solution Development

In this section, we propose ordinary differential equations (ODEs) of the multi-compartment system coupled with radionuclide decay/ingrowth networks and source-term activities, and derive closed-form solutions for given network structures (Fig. 2, see also Bourret et al., 2021). The study domain is composed of multiple compartments (gas-filled cavity, melt puddle, and host rock) connected by inter-compartment mass exchange (precursor rainout, seepage from gas-filled cavity to host rock, and/or prompt venting from the cavity to ground surface).

The mass change of all radionuclides in each decay chain in the multi-compartment system described in Fig. 1 can be expressed as

$$\frac{d}{dt}\begin{bmatrix} \mathbf{c}_c \\ \mathbf{c}_p \\ \mathbf{c}_h \\ \mathbf{c}_v \end{bmatrix} = \begin{bmatrix} \mathbf{A} - \mathbf{R} - \mathbf{S} - \mathbf{Q} & \mathbf{O} & \mathbf{O} & \mathbf{O} \\ \mathbf{R} & \mathbf{A} & \mathbf{O} & \mathbf{O} \\ \mathbf{S} & \mathbf{O} & \mathbf{A} & \mathbf{O} \\ \mathbf{Q} & \mathbf{O} & \mathbf{O} & \mathbf{A} \end{bmatrix}\begin{bmatrix} \mathbf{c}_c \\ \mathbf{c}_p \\ \mathbf{c}_h \\ \mathbf{c}_v \end{bmatrix},$$
$$(1)$$

where $\mathbf{c}_c$, $\mathbf{c}_p$, $\mathbf{c}_h$, and $\mathbf{c}_v$ are the mass vectors in cavity, puddle, host rock, and prompt release, respectively. $\mathbf{A}$ is a matrix of the first-order decay and ingrowth rates, $\mathbf{R}$ is the rainout-rate matrix from cavity to puddle, $\mathbf{S}$ is the seepage-rate matrix, and $\mathbf{Q}$ is the prompt venting matrix. $\mathbf{O}$ denotes $n \times n$ zero matrices and n is the number of radionuclides in the decay chain.
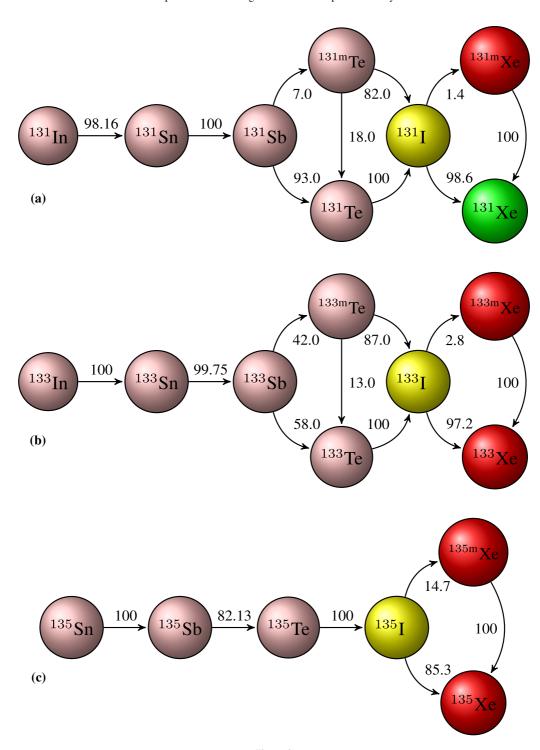
Figure 2
Radioactive xenon decay/ingrowth networks of decay chains **a** 131, **b** 133, and **c** 135. Numbers on arrows denote branching factor (%). Red and green icons represent radioactive and stable xenon isotopes while pink and yellow icons denote precipitating and possible precipitating precursors. The decay networks are based on England and Rider (1994)

2.1. Cavity Temperature

The residual heat of a UNE is translated into a temperature distribution in the cavity and surrounding area. The post-shot temperature distribution can be estimated with a Hugoniot phenomenological equation of state model, as described by Butkovich (1974):

$$T = T_0 + \frac{8.95 \times 10^5}{\rho^{3.156}} \left(\frac{R}{Y^{\frac{1}{3}}} \right)^{-4.576\, \rho^{-0.411}}, \qquad (2)$$

where T [°C] is the temperature, T_0 [°C] is the initial temperature prior to detonation, R [m] is the radial distance from the working point (in a spherical coordinate system), Y [kt] is the energy-equivalent yield, and ρ [g cm^{-3}] is the bulk density of the rock. A simple Newtonian cooling is assumed (Olsen, 1967) for calculating the rainout time as

$$t = \frac{1}{\beta} \ln \frac{T_m - T_0}{T_c - T_0}, \qquad \beta = \frac{\ln 2}{t_{T/2}} \qquad (3)$$

where T_m [°C] is the post-shot temperature in the cavity, T_c [°C] is the condensation temperature, β is the temperature decay factor, and $t_{T/2}$ is the half-time of cavity temperature. Using (2) and assuming a cavity radius of 20 m, the cavity temperature can be calculated as shown in Fig. 3a for an uncompacted soil (1.2 g cm^{-3}) and two denser rock types with three different rock densities. The corresponding
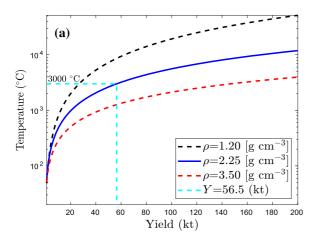
rainout times of In, Sn, Sb, and Te-m/Te are shown in Fig. 3b.

2.2. Precipitation of Precursors

The post-detonation precipitation of the refractory radioactive inventory involves a time-dependent mass transfer from the vapor-filled cavity to the rock melt or puddle at the bottom of the cavity. This is a complex problem that is dependent on several parameters (e.g., cavity pressure, temperature, yield, cavity-gas composition, etc.) and for the purposes of this paper only a somewhat general and simplified model is considered here. It is assumed that during the rapid cooling of the post-detonation vapor phase as described in Sect. 2.1, the vaporized iodine precursors (In, Sn, Sb, Te-m, and Te) condense out, mixing with the melt phase in the puddle compartment (Pili et al., 2017; Carrigan et al., 2020). Since no significant short-term diffusion mechanism has been identified from the puddle to cavity (Carrigan et al., 2020), any back diffusion from the puddle to the cavity gas is neglected. The rainout is expressed as

$$\frac{d}{dt} \begin{bmatrix} \mathbf{c}_c \\ \mathbf{c}_p \end{bmatrix} = \begin{bmatrix} -\mathbf{R} & \mathbf{O} \\ \mathbf{O} & \mathbf{R} \end{bmatrix} \begin{bmatrix} \mathbf{c}_c \\ \mathbf{c}_c \end{bmatrix}, \qquad (4)$$

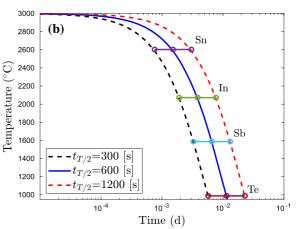where $\mathbf{R}$ is a diagonal rainout-rate matrix. For

Figure 3
a Cavity temperature versus yield number in three different geologic conditions. **b** Rainout schedule of iodine precursors under Newtonian cooling

example, the rainout-rate matrix of decay chain 131 (Fig. 2a) can be specified as

$$\mathbf{R} = \text{diag} \quad (\overbrace{\mathcal{H}(T_1)r_1}^{^{131}\text{In}} \quad \overbrace{\mathcal{H}(T_2)r_2}^{^{131}\text{Sn}} \quad \overbrace{\mathcal{H}(T_3)r_3}^{^{131}\text{Sb}}$$
$$\overbrace{\mathcal{H}(T_4)r_4}^{^{131m}\text{Te}} \quad \overbrace{\mathcal{H}(T_4)r_5}^{^{131}\text{Te}} \quad \overbrace{0 \ \ 0 \ \ 0}^{\text{daughters}})$$

(5)

where T_i, $i = 1, 2, 3, 4$, are the assumed condensation temperatures of In, Sn, Sb, and Te-m/Te, respectively, r_i, $i = 1, \ldots, 5$, are rainout rates, and $\mathcal{H}(T_i)$ is the Heaviside step function with $\mathcal{H}(T_i) = 0$, $\forall \, T > T_i$ and $\mathcal{H}(T_i) = 1$, $\forall \, T \leq T_i$.

2.3. Seepage of Isotopic Xenon

It is also assumed that xenon isotopes produced in the cavity transport away to the host rock, and the mass loss from the cavity, due to excess pressure, is linearly proportional to the mass in the cavity, which is consistent with the ideal gas law. The mass change is expressed as

$$\frac{d}{dt} \begin{bmatrix} \mathbf{c}_c \\ \mathbf{c}_h \end{bmatrix} = \begin{bmatrix} -\mathbf{S} & \mathbf{O} \\ \mathbf{O} & \mathbf{S} \end{bmatrix} \begin{bmatrix} \mathbf{c}_c \\ \mathbf{c}_c \end{bmatrix},$$

(6)

where $\mathbf{S}$ is the diagonal matrix representing the seepage rates of xenon isotopes from cavity to host rock. For decay chain 131, $\mathbf{S}$ in Eq. (6) is specified as

$$\mathbf{S} = \text{diag} \quad (\overbrace{0 \ \ 0 \ \ 0 \ \ 0 \ \ 0 \ \ 0}^{\text{precursors}} \quad \overbrace{s_1}^{^{131m}\text{Xe}} \quad \overbrace{s_2}^{^{131}\text{Xe}}),$$

(7)

where s_1 and s_2 are seepage rates of ^{131m}Xe and ^{131}Xe.

2.4. Prompt Venting of Isotopic Xenon

Prompt release (venting) driven by pressure gradient (between the cavity and ground surface) is described by one-dimensional advection and expressed in the form of first-order reaction

$$\frac{\partial \mathbf{c}_c}{\partial t} = -\Pi(t_0, t_1) \, v \frac{d\mathbf{c}_c}{dx} = -\Pi(t_0, t_1) \, \frac{v}{L} (\mathbf{c}_c - 0)$$
$$= -\Pi(t_0, t_1) \, q \, \mathbf{c}_c$$

(8)

where v [m s^{-1}] is the velocity of venting flow, L [m] is the venting distance, q [s^{-1}] is the mass loss rate due to prompt venting, and $\Pi(t_0, t_1)$ [–] is a boxcar function defined as

$$\Pi(t_0, t_1) = \begin{cases} 0, & t < t_0 \\ 1, & t_0 \leq t \leq t_1 \\ 0, & t > t_1. \end{cases}$$

The mass change due to the prompt venting is described in matrix format as

$$\frac{d}{dt} \begin{bmatrix} \mathbf{c}_c \\ \mathbf{c}_v \end{bmatrix} = \begin{bmatrix} -\mathbf{Q} & \mathbf{O} \\ \mathbf{O} & \mathbf{Q} \end{bmatrix} \begin{bmatrix} \mathbf{c}_c \\ \mathbf{c}_c \end{bmatrix}.$$

(9)

For decay chain 131, $\mathbf{Q}$ in Eq. (9) is specified as

$$\mathbf{Q} = \text{diag} \quad (\overbrace{0 \ \ 0 \ \ 0 \ \ 0 \ \ 0 \ \ 0}^{\text{precursors}} \quad \overbrace{\Pi(t_0, t_1) \, q}^{^{131m}\text{Xe}} \quad \overbrace{\Pi(t_0, t_1) \, q}^{^{131}\text{Xe}}),$$

(10)

where t_0 and t_1 [s] are the starting and ending time of prompt venting.

2.5. Solution Development

Equation (1) is arranged as a lower triangular matrix

$$\frac{d\mathbf{c}}{dt} = \mathscr{A} \, \mathbf{c}, \quad \mathbf{c} = [\mathbf{c}_c; \mathbf{c}_p; \mathbf{c}_h; \mathbf{c}_v]$$

(11)

where $\mathscr{A}$ is lumped matrix diagonalized as

$$\mathscr{A} = \mathcal{S} \Lambda \mathcal{S}^{-1}$$

(12)

where Λ is an eigenvalue matrix of $\mathscr{A}$, $\mathcal{S}$ is the matrix whose columns are the eigenvectors of $\mathscr{A}$, and $\mathcal{S}^{-1}$ is the inverse matrix of $\mathcal{S}$. The analytical formulation of $\mathcal{S}$ and $\mathcal{S}^{-1}$ is described in Sun et al. (2012, 2015, and 2021).

Defining $\mathbf{a} = \mathcal{S}^{-1}\mathbf{c}$, Eq. (11) is expressed in terms of $\mathbf{a}$ as

$$\frac{d\mathbf{a}}{dt} = \Lambda \, \mathbf{a}$$

(13)

with a transformed initial condition $\mathbf{a}^0 = \mathcal{S}^{-1}\mathbf{c}^0$

Table 1

Deterministic models with multiple physical processes

Model	Chain reactions A [s^{-1}]	Rainout r [s^{-1}]	Seepage s [s^{-1}]	Prompt venting q [s^{-1}]
0	☑	☐	☐	☐
1	☑	☑ 1.0×10^{-3}	☐	☐
2	☑	☐	☑ 5.0×10^{-5}	☐
3	☑	☐	☐	☑ 1.0×10^{-2}
4	☑	☑ 1.0×10^{-3}	☑ 5.0×10^{-5}	☑ 1.0×10^{-2}

where $\mathbf{c}^0$ is the vector of initial concentrations. Each ODE in Eq. (13) is independent of the others, but with the first-order decay rate λ. In other words, the coupled ODEs (Eq. 11) in terms of $\mathbf{c}$ by ingrowth, rainout, seepage, and prompt venting, are decomposed into N ODEs with the same formulation,

$$\frac{da_i}{dt} = \lambda_i\, a_i, \quad \forall i = 1, 2, \ldots, N, \qquad (14)$$

where a_i is the transformed concentration of c_i and the solution of a_i is

$$a_i = a_i^0 \exp(\lambda_i t), \quad \forall i = 1, 2, \ldots, N. \qquad (15)$$

Using $\mathbf{c} = \mathcal{S}\,\mathbf{a}$, the solution of $\mathbf{c}$ is

$$\mathbf{c}(t) = \mathcal{S} \begin{bmatrix} \exp(\lambda_1 t) & 0 & \cdots & 0 \\ 0 & \exp(\lambda_2 t) & \cdots & 0 \\ \vdots & \vdots & \ddots & \vdots \\ 0 & \cdots & 0 & \exp(\lambda_N t) \end{bmatrix} \mathcal{S}^{-1}\,\mathbf{c}^0, \qquad (16)$$

The closed-form solution can be verified for absolutely sequential reactions by comparing the Bateman equation (Bateman, 1910) and for an integrated system (with all source-term activities) by comparing a numerical solution using ode113s in MATLAB (MathWorks, 2000).

3. Results and Analyses

In this section, we simulate the evolution of xenon isotopes in the cavity, melt puddle, host-rock, and promptly vented gas, and xenon isotopic ratios for demonstrating the impact of source-term activities on

xenon signatures. Assuming zero initial inventory in the puddle for 1 kt U235 fission, four models are conceptualized as listed in Table 1 for demonstrating the effect of source-term processes on xenon inventories and isotopic ratios of activities. A reference model (#0) representing the idealized case of isotopic evolution in a cavity determined entirely by the radioactive decay chain (Kalinowski et al., 2010; Kalinowski, 2011; Yamba et al., 2016) is used to compare models #1, 2, 3 for demonstrating the individual effect of rainout, seepage, and prompt venting, respectively. Model #4 includes all four processes (Table 1)

3.1. Evolution of Xenon Isotopes

Assuming the cavity temperature decaying from 3000 to 20 °C with temperature half-life of 600 [s] and a prompt venting between 1×10^5 [s] (1.16 [d]) and 1.864×10^5 [s] (2.16 [d]), the xenon inventories of Model #4 in the cavity and promptly vented gas were simulated as shown in Fig. 4.

As shown in Fig. 4a–c, the xenon inventories in the cavity are clearly reduced due to the prompt venting between 10^5 and 1.864×10^5 [s]. ^{135}Xe in vented gas peaks during the venting period due to its short half-life, while other three xenons peak after the one-day venting (Fig. 4d). A late-time venting may not contain detectable signature ^{135}Xe because of its short half-life. The inventory profiles shown in Fig. 4 can be used to calculate isotopic ratios of xenon radioactivities. Fig. 5a shows the Multi-Isotope Ratio Chart (MIRC, the correlation of ^{133m}Xe/^{131m}Xe and ^{135}Xe/^{133}Xe) in the cavity and host rock with individual and combined source activities. While
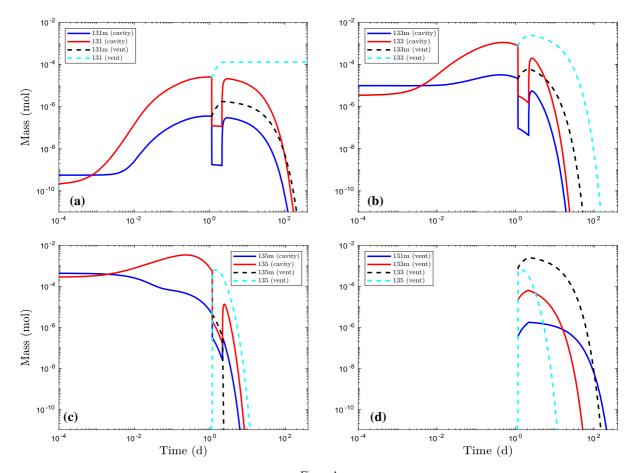
Figure 4
Inventories of xenon isotopes in cavity and promptly vented gas. **a** ^{131m}Xe and ^{131}Xe. **b** ^{133m}Xe and ^{133}Xe. **c** ^{135m}Xe and ^{135}Xe. **d** ^{131m}Xe, ^{133m}Xe, ^{133}Xe, and ^{135}Xe in promptly vented gas

rainout shifts the England and Rider curve (blue) to the right (see also Carrigan et al., 2020), seepage (cyan) and prompt venting (dashed magenta) move the curve back to the left on the plot. The time-dependent ratio of ^{131m}Xe to ^{133}Xe (in the cavity) shown in Fig. 5b indicates that rainout brings the England and Rider (ER) curve (Model #0, blue) down toward the *x*-axis while both seepage and prompt venting lift the ratio value above the blue curve under the ER condition. The comparison between observed data and Model #0 curve reveals if the system is closed with rainout or open with possible seepage or prompt venting.

The observed data of ^{131m}Xe/^{133}Xe ratio from atmospheric samples associated with the February 2013 declared DPRK UNE at the Punggye-ri Nuclear Test Site, with a known detonation time (Ringbom et al., 2014), may indicate the precursor precipitation occurred in a leaky system. Three Japanese data sets that are located below the ER curve (blue curve) and close to the ^{131m}Xe/^{133}Xe ratio in host rock (green curve) reflect a possible seepage from the cavity to host rock since those samples were taken off site. Both ^{131m}Xe/^{133}Xe ratios in cavity (red curve) and host rock (green curve) behave similarly after 0.2 d in this example. If those samples (circles) were taken from the cavity directly, the red curve might be used to interpret the early-time precipitation. Two Russian data points (green squares) located above the ER curve may indicate a possible venting from the cavity.
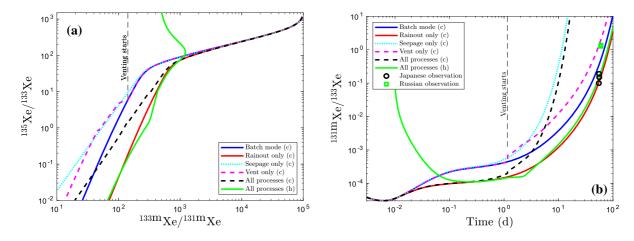
Figure 5
a Correlation of xenon isotopic ratios between $^{133m}Xe/^{131m}Xe$ and $^{135}Xe/^{133}Xe$, and **b** ratio of $^{131m}Xe/^{133}Xe$ versus time in the cavity. The vertical dashed lines in both **a** and **b** indicate the starting time of prompt venting. '(c)' and '(h)' in figure legends indicate model results in cavity and host rock, respectively

3.2. Effect of Rainout on Xenon Activity Ratios

In absence of seepage and prompt venting, the rainout effect on both MIRC and $^{131m}Xe/^{133}Xe$ ratio in the cavity is simulated using Model #1 and shown in Fig. 6a, b for three different rainout rates [1×10^{-4}, 1×10^{-3}, 1×10^{-2}] [s^{-1}] under Newtonian cooling condition from 3000 to 20 °C with temperature half-life of 600 [s]. As shown in Fig. 6a, a fast rainout moves the correlation to the right away from the ER curve (batch-mode closed without rainout). Similarly, the fast rainout results in a low ratio of $^{131m}Xe/^{133}Xe$ (Fig. 6b). In addition to the rainout-rate effect, the temperature profile also affects MIRC and $^{131m}Xe/^{133}Xe$ ratio. Fig. 6c, d show the MIRC and $^{131m}Xe/^{133}Xe$ ratio for $t_{T/2} = [300\ 600\ 1200]$ [s] and $r = 1 \times 10^{-3}$ [s^{-1}]. All possible rainout scenarios (for given r and $t_{T/2}$) move both MIRC and $^{131m}Xe/^{133}Xe$ ratio to the right side of their ER curves.

3.3. Effect of Seepage and Prompt Venting on Xenon Activity Ratios

When s is assumed to be [1×10^{-6}, 1×10^{-5}, 1×10^{-4}] [s^{-1}] without considering rainout and prompt venting, the MIRC and $^{131m}Xe/^{133}Xe$ ratio in the cavity are simulated using Model #2 as shown in Fig. 7a, b. A high seepage rate moves the MIRC correlation away from the ER curve towards the left

and produces $^{131m}Xe/^{133}Xe$ ratio higher than the curve subject to idealized batch-mode conditions. Similarly to seepage effect, the time of prompt venting (Model #3) deviates the MIRC (Fig. 7c) and $^{131m}Xe/^{133}Xe$ ratio (Fig. 7d) curves away from the standard ER curves after the prompt venting starts. Although a different venting rate q alters xenon inventories in the cavity, it does not change the MIRC and $^{131m}Xe/^{133}Xe$ ratio. The time scale of seepage and venting is referred to OTA (1989).

4. Discussion and Conclusion

For predicting time-dependent isotopic evolution, the idealized standard model (ER) assuming a batch-mode closed cavity may not be appropriate when iodine precursors precipitate from the cavity to the melt puddle, xenon isotopes transport to host rock, or prompt venting occurs. We extended our closed-form solution to a multi-compartment system coupled with complex radioactive decay/ingrowth networks, temperature-dependent precursor precipitation, cavity gas seepage, and specified prompt venting. The standard model (#0 in Table 1) serves as a reference with deviations potentially indicating precipitation of refractories, xenon seepage, and/or prompt venting have occurred and if the cavity is closed. For
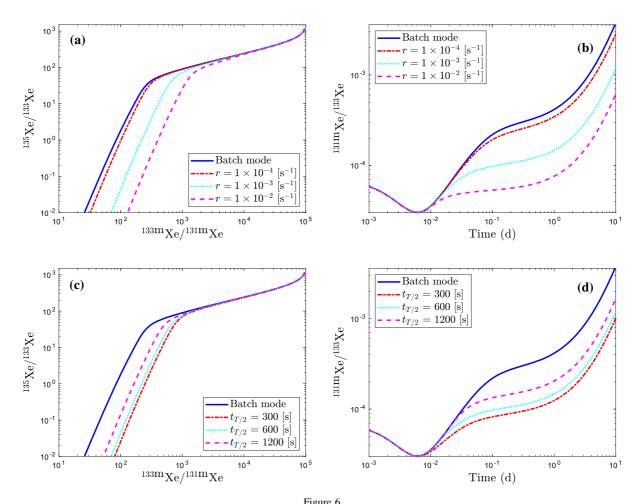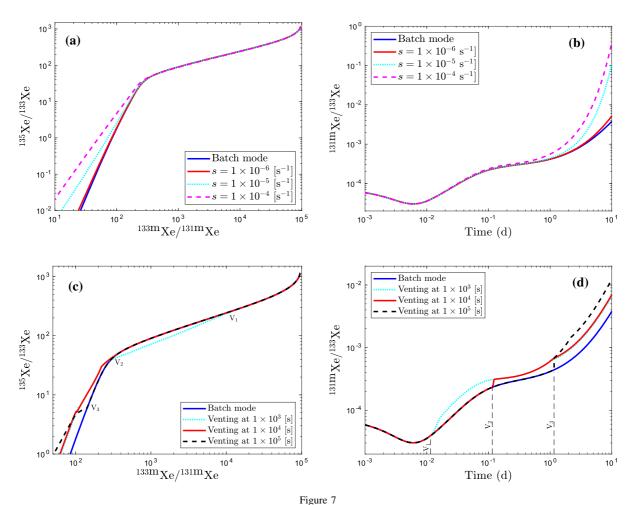
Figure 6

a Effect of rainout rate on MIRC with $t_{T/2} = 600$ [s]. **b** Ratio of ^{131m}Xe/^{133}Xe versus time with different rainout rates with $t_{T/2} = 600$ [s]. **c** Effect of temperature half-life on MIRC with $r = 1 \times 10^{-3}$ [s^{-1}]. **d** Ratio of ^{131m}Xe/^{133}Xe versus time with different temperature half-lives (Fig. 3b) with $r = 1 \times 10^{-3}$ [s^{-1}]

example, data points of cavity samples located above the ER curve in ^{131m}Xe/^{133}Xe(t) (Fig. 5b) indicate possible seepage or prompt venting while those data points of the cavity samples below the ER curve demonstrate an early-time precipitation of iodine precursors. Only early-time processes (i.e., precipitation, seepage, and prompt venting) under thermal conditions are considered in our model and analytical solution. Late-time driving force of gas transport (e.g., barometric pumping) in fractured rock is not considered. A prompt venting that can be physically defined by operational activities (e.g., starting and ending time), uncertain hydrodynamic and geological conditions (e.g., depth of burial, rock properties,

venting pathways) is described by venting rate q with a boxcar function ($\Pi(t_0, t_1)$ in Eq. 8). Although the Newtonian cooling is used in this paper for describing the fast cooling processes (from 3000 to 988 °C), the true temperature profile either from an onsite monitoring or hydrodynamic modeling can be inputted to calculate precursor precipitation schedule. Then, the difference between observed xenon activity ratios and those simulated using ER model may be possibly used to calculate yield number inversely and recover historic source-term activities. If the cavity temperature remains above 988 °C for a long time (e.g., $t_{T/2} > 100$ [d]), the precursors of iodine will have enough time to decay away for complete xenon

Figure 7
a Effect of seepage on MIRC. **b** Effect of seepage on $^{131m}Xe/^{133}Xe$ ratio. **c** Effect of venting time on MIRC. **d** Effect of venting time on $^{131m}Xe/^{133}Xe$ ratio. Venting duration is 1 day and venting rate is 1×10^{-2} [s^{-1}]

production in the cavity and the effect of rainout is eliminated. Then, the analytical solution with $r \simeq 0$ applies for seepage and prompt venting only. The generalized analytical solution can be used as a handy and robust tool for conducting sensitivity analyses and verifying high-fidelity computer codes with a low computational cost.

In this paper, we have only considered precipitation of the refractory precursors of iodine. We have assumed most or all iodine remains in the cavity gas phase and does not precipitate into the underlying melt or onto hot cavity surfaces. Such an assumption is probably justifiable for gas seepage rather than for rapid venting. If rapid venting occurs, it is expected that isotopes of iodine may be released with

radioxenon, which will have the effect of shifting the MIRC toward the ER ingrowth curve and away from the rainout curve. Future analytical models will attempt to quantify this effect of iodine loss during the period of rapid venting.

of Energy and performed under the auspices of the US Department of Energy by Lawrence Livermore National Laboratory under Contract number DE-AC52-07NA27344. The authors acknowledge important interdisciplinary collaboration with scientists and engineers from Los Alamos National Laboratory, Lawrence Livermore National Laboratory, Mission Support and Test Services, Pacific Northwest National Laboratory, and Sandia National Laboratories. The authors greatly appreciate Léa Pannecoucke for the initial discussion on gas-magma interactions that stimulated the model development in this paper.

Declarations

Conflict of interest The authors declare that they have no known competing financial interests or personal relationships that could have appeared to influence the work reported in this paper.

Publisher's Note Springer Nature remains neutral with regard to jurisdictional claims in published maps and institutional affiliations.

References

Achim, P., Generoso, S., Morin, M., Gross, P., Le Petit, G., & Moulin, C. (2016). Characterization of Xe-133 global atmospheric background: Implications for the international monitoring system of the comprehensive nuclear-test-ban treaty. *Journal of Geophysical Research: Atmospheres, 121,* 4951–4966.

Bateman, H. (1910). Solution of a system of differential equations occurring in the theory of radioactive transformations. *Proceedings of the Cambridge Philosophical Society, 15,* 423–427.

Bourret, S. M., Kwicklis, T. A., & Stauffer, P. H. (2021). Evaluation of several relevant fractionation processes as possible explanation for radioxenon isotopic activity ratios in samples taken near underground nuclear explosions in shafts and tunnels. *Journal of Environmental Radioactivity, 237,* 106698.

Bowyer, T. W. (2020). A review of global radioxenon background research and issues. *Pure and Applied Geophysics.* https://doi.org/10.1007/s00024-020-02440-0.

Bowyer, T. W., Abel, K. H., Hubbard, C. W., McKinnon, A. D., Panisko, M. E., Perkins, R. W., et al. (1998). Automated separation and measurement of radioxenon for the Comprehensive Test Ban Treaty. *Journal of Radioanalytical and Nuclear Chemistry, 235,* 77–82.

Butkovich, T. R. (1974). Rock melt from an underground nuclear explosion. University of California, Lawrence Livermore Laboratory, Report UCRL-51554.

Carrigan, C. R., Sun, Y., Hunter, S., Ruddle, D., Wagoner, J., Myers, K., et al. (2016). Delayed signatures of underground nuclear explosions. *Scientific Reports, 6,* 1–9. https://doi.org/10.1038/srep23032.

Carrigan, C. R., Sun, Y., Pili, E., Neuville, D., & Antoun, T. (2020). Cavity-melt partitioning of refractory radionuclides and implications for detecting underground nuclear explosions. *Journal of Environmental Radioactivity, 219,* 106269. https://doi.org/10.1016/j.jenvrad.2020.106269.

Carrigan, C. R., Sun, Y., Pili, E., Neuville, D., & Antoun, T. (2021). Implications of underground nuclear explosion cavity evolution for radioxenon isotopic composition. CTBT Science and Technology 2021 (SnT2021), June 28, 2021.

De Geer, L.-E. (2013). Reinforced evidence of a low-yield nuclear test in North Korea on 11 May 2010. *Journal of Radioanalytical and Nuclear Chemistry, 298,* 2075–2083.

England, T. R., & Rider, B. F. (1994). ENDF-349 evaluation and compilation of fission product yields 1993. Los Alamos National Laboratory, LA-UR-94-3106.

Galan, M., Kalinowski, M., Gheddou, A., & Yamba, K. (2018). New evaluated radioxenon decay data and its implications in nuclear explosion monitoring. *Journal of Environmental Radioactivity, 192,* 628–634.

Gueibe, C., Kalinowski, M. B., Baré, J., Gheddou, A., Krysta, M., & Kusmierczyk-Michulec, J. (2017). Setting the baseline for estimated background observations at IMS systems of four radioxenon isotopes in 2014. *Journal of Environmental Radioactivity, 178–179,* 297–314.

Haas, D. A., Eslinger, P. W., Bowyer, T. W., Cameron, I. M., Hayes, J. C., Lowrey, J. D., & Miley, H. S. (2017). Improved performance comparisons of radioxenon systems for low level releases in nuclear explosion monitoring. *Journal of Environmental Radioactivity, 178–179,* 127–135.

Hoffman, I., & Berg, R. (2018). Medical isotope production, research reactors and their contribution to the global xenon background. *Journal of Radioanalytical and Nuclear Chemistry, 318*(1), 165–173. https://doi.org/10.1007/s10967-018-6128-2.

Kalinowski, M. B. (2011). Characterisation of prompt and delayed atmospheric radioactivity releases from underground nuclear tests at Nevada as a function of release time. *Journal of Environmental Radioactivity, 102,* 824–836.

Kalinowski, M. B., Axelsson, A., Bean, M., Blanchard, X., Bowyer, T. W., Brachet, G., et al. (2010). Discrimination of nuclear explosions against civilian sources based on atmospheric xenon isotopic activity ratios. *Pure and Applied Geophysics, 167*(4–5), 517–539.

Kalinowski, M. B., & Liao, Y.-Y. (2014). Isotopic characterization of radioiodine and radioxenon in releases from underground

nuclear explosions with various degrees of fractionation. *Pure and Applied Geophysics, 171*(3), 677–692.

Kalinowski, M. B., & Pistner, C. J. (2006). Isotopic signature of atmospheric xenon released from light water reactors. *Journal of Environmental Radioactivity, 88,* 215–235.

Le Petit, G., Cagniant, A., Gross, P., Douysset, G., Topin, S., Fontaine, J. P., et al. (2015). $\text{ Spalax}^{{\rm TM}}$ new generation: A sensitive and selective noble gas system for nuclear explosion monitoring. *Applied Radiation and Isotopes, 103,* 102–114.

MathWorks. (2000). *MATLAB high-performance numeric computation and visualization software*. Web site: http://www.mathwroks.com. Natick, MA, USA.

Olsen, C. W. (1967). Time history of the cavity pressure and temperature following a nuclear detonation in alluvium. *Journal of Geophysical Research, 72*(20), 5037–5041. https://doi.org/10.1029/JZ072i020p05037.

Pili, E., Pannecoucke, L., Guillon, S., & Neuville, D. R. (2017). Gas–magma interactions in nuclear cavities and their effects on the xenon isotopes. CTBT Science and Technology 2017 Conference, Vienna, Austria.

Ringbom, A., Axelsson, A., Aldener, M., Bowyer, T. W., Fritioff, T., Hoffman, I., et al. (2014). Radioxenon detections in the CTBT international monitoring system likely related to the announced nuclear test in North Korea on February 12, 2013. *Journal of Environmental Radioactivity, 128,* 47–63.

Saey, P. R. J., Bowyer, T. W., & Ringbom, A. (2010). Isotopic noble gas signatures released from medical isotope production facilities—Simulations and measurements. *Applied Radiation and Isotopes, 68*(9), 1846–1854.

Saey, P. R. J., & De Geer, L.-E. (2005). Notes on radioxenon measurements for CTBT verification purposes. *Applied Radiation and Isotopes, 63,* 765–773.

Sloan, J., Sun, Y., & Carrigan, C. (2016). Uncertainty quantification for discrimination of nuclear events as violations of the comprehensive nuclear-test-ban treaty. *Journal of Environmental Radioactivity, 155,* 130–139.

Sun, Y., Buscheck, T. A., & Hao, Y. (2012). An analytical method for modeling first-order decay networks. *Computers and Geosciences, 39,* 86–97.

Sun, Y., Carrigan, C., Cassata, W., Hao, Y., Ezzedine, S., & Antoun, T. (2021). A closed-form solution for source-term emission of xenon isotopes from underground nuclear explosions. *Transport in Porous Media, 139,* 131–153. https://doi.org/10.1007/s11242-021-01650-x.

Sun, Y., Carrigan, C. R., & Hao, Y. (2015). Radioxenon production and transport from an underground nuclear detonation to ground surface. *Pure and Applied Geophysics, 172,* 243–265.

U.S. Congress, Office of Technology Assessment. (1989). The containment of underground nuclear explosions. OTA-ISC-414, Washington, D.C.

Yamba, K., Sanogo, O., Kalinowski, M. B., Nikkinen, M., & Koulidiati, J. (2016). Fast and accurate dating of nuclear events using La-140/Ba-140 isotopic activity ratio. *Applied Radiation and Isotopes, 112,* 141–146.